INSTITUTE OF PHYSICS PUBLISHING JOURNAL OF PHYSICS: CONDENSED MATTER

J. Phys.: Condens. Matter **13** (2001) 2377–2394 www.iop.org/Journals/cm PII: S0953-8984(01)16928-6

Two-photon excitation spectroscopy of Cr^{3+}:K_2NaScF_6 elpasolite: II. Theoretical models

R H Bartram, G R Wein[1] **and D S Hamilton**

Department of Physics and Institute of Materials Science, University of Connecticut, Storrs, CT 06269-3046, USA

Received 7 September 2000, in final form 8 January 2001

Abstract

Two-photon excitation (TPE) spectra of Cr^{3+}:K_2NaScF_6, excited by a Raman-shifted, Nd:YAG-pumped tunable dye laser, exhibit several unexpected features. A weak TPE spectrum of the symmetry-forbidden $^4A_{2g} \rightarrow {}^4T_{2g}$ transition is observed without a zero-phonon line. The symmetry-allowed TPE spectrum of the $^4A_{2g} \rightarrow {}^4T_{1ag}$ transition has a multi-phonon side band with anomalously extended vibrational progressions, and an anomalously weak, split zero-phonon line with anomalous polarization anisotropy. These observations are explained, respectively, in terms of theoretical models involving phonon assistance, departures from the closure approximation that permit electron–lattice coupling in intermediate states and a low-temperature phase transition involving librational instability. Hypothetical line-shape simulations are compared with observed TPE spectra.

1. Introduction

Two-photon excitation (TPE) spectra of Cr^{3+}:K_2NaScF_6 presented in the preceding paper [1], henceforth designated I, exhibit several unexpected features. A phonon side band associated with the symmetry-forbidden $^4A_{2g} \rightarrow {}^4T_{2g}$ transition is observed despite the absence of a zero-phonon line. The TPE spectrum associated with the $^4A_{2g} \rightarrow {}^4T_{1ag}$ transition has anomalously extended progressions and a split zero-phonon line with anomalous polarization anisotropy. The purpose of the present paper is to develop theoretical models for TPE spectra that address these anomalous features.

The theory of two-photon absorption (TPA) was first discussed by Göppert-Mayer [2]. Its experimental realization in solids [3], following the advent of the ruby laser, stimulated further theoretical development. The closure approximation for intermediate states was introduced as a simplifying assumption by Axe [4]. Selection rules and polarization anisotropy were investigated by Inoue and Toyozawa [5] and extended by Bader and Gold [6]. Phonon-assisted TPA was considered by Gold and Hernandez [7] and by Honig *et al* [8]. All of these developments are relevant to the interpretation of the present experiment.

---

[1] Present address: St George's School, PO Box 1910, Newport, RI 02840, USA.

0953-8984/01/102377+18$30.00

The transition probability in second-order, time-dependent perturbation theory for a two-photon transition between electronic states a and b, induced by light of intensity I_0, angular frequency ω and polarization $\hat{\boldsymbol{\eta}}$, is

$$W_{a\to b} = F(I_0)\left|\sum_c \frac{\langle \mathrm{b}|\hat{\boldsymbol{\eta}}\cdot\boldsymbol{R}|\mathrm{c}\rangle\langle \mathrm{c}|\hat{\boldsymbol{\eta}}\cdot\boldsymbol{R}|\mathrm{a}\rangle}{\omega_{ca}-\omega}\right|^2 \delta(\omega_{ba}-2\omega) \tag{1a}$$

$$F(I_0) = \left[\frac{(n^2+2)^2}{9n}\right]^2\left(\frac{\pi e^4 I_0^2}{2\varepsilon_0^2 c^2\hbar^4}\right) \tag{1b}$$

$$\boldsymbol{R} \equiv \sum_i \boldsymbol{r}_i \tag{1c}$$

where $\boldsymbol{r}_i$ is the position operator of the ith electron. The closure approximation [4] is obtained by assuming a common energy denominator, $\omega_{ca}-\omega \cong \Delta$, for all intermediate states,

$$W_{a\to b} = [F(I_0)/\Delta^2]\times|\langle \mathrm{b}|(\hat{\boldsymbol{\eta}}\cdot\boldsymbol{R})^2|\mathrm{a}\rangle|^2\delta(\omega_{ba}-2\omega). \tag{2}$$

This formalism can be extended readily to vibronic states in the Born–Oppenheimer approximation [9], appropriate to non-degenerate electronic states,

$$\psi_{nv}(\boldsymbol{r},\boldsymbol{Q}) \cong \phi_n(\boldsymbol{r},\boldsymbol{Q})\theta_{nv}(\boldsymbol{Q}) \tag{3a}$$

$$[T_e + V(\boldsymbol{r},\boldsymbol{Q}) - U_n(\boldsymbol{Q})]\phi_n(\boldsymbol{r},\boldsymbol{Q}) = 0 \tag{3b}$$

$$[T_N + U_n(\boldsymbol{Q}) - E_{nv}]\theta_{nv}(\boldsymbol{Q}) = 0 \tag{3c}$$

where T_e and T_N are electronic and nuclear kinetic energy operators, respectively, $\boldsymbol{r}$ denotes electronic coordinates and $\boldsymbol{Q}$ denotes mass-weighted nuclear coordinates. In the harmonic approximation,

$$V(\boldsymbol{r},\boldsymbol{Q}) \cong V(\boldsymbol{r},\boldsymbol{0}) + \sum_k V_k Q_k + \tfrac{1}{2}\sum_k \omega_k^2 Q_k^2 \tag{4a}$$

$$V_k \equiv (\partial V/\partial Q_k)_{\boldsymbol{Q}=\boldsymbol{0}} \tag{4b}$$

the vibrational wave function may be written as a function of normal coordinates Q_k,

$$\theta_{nv}(\boldsymbol{Q}) = \prod_k \chi_{v_k}(Q_k - Q_{0k}^{(n)}) \equiv \prod_k \chi_{nv_k}(Q_k) \tag{5a}$$

$$Q_{0k}^{(n)} = \langle n|V_k|n\rangle/\omega_k^2 \tag{5b}$$

where $\chi_{v_k}(Q_k)$ is the wave function for a simple harmonic oscillator of angular frequency ω_k.

A further simplification is achieved by neglecting the dependence of the electronic wave function on nuclear coordinates (crude adiabatic approximation),

$$\phi_n(\boldsymbol{r},\boldsymbol{Q}) \cong \phi_n(\boldsymbol{r},\boldsymbol{0}). \tag{6}$$

Within the closure, Born–Oppenheimer, harmonic and crude-adiabatic approximations, the TPA transition probability is given by

$$W_{a\to b} = [F(I_0)/\Delta^2]\times|\langle \mathrm{b}|(\hat{\boldsymbol{\eta}}\cdot\boldsymbol{R})^2|\mathrm{a}\rangle|^2 G(\Omega) \tag{7}$$

where $G(\Omega)$ is a normalized line-shape function,

$$G(\Omega) = \mathrm{Av}_{\{\alpha_k\}}\sum_{\{\beta_k\}}\prod_k |\langle\chi_{b\beta_k}\mid\chi_{a\alpha_k}\rangle|^2\delta\left[\sum_k(\beta_k-\alpha_k)\omega_k - \Omega\right] \tag{8a}$$

$$\Omega = 2\omega - \Omega_0 \tag{8b}$$

$$\Omega_0 = \hbar^{-1}[U_b(Q_0^{(b)}) - U_a(Q_0^{(a)})] \tag{8c}$$

where $\{\alpha_k\}$ and $\{\beta_k\}$ denote sets of vibrational quantum numbers and where $\mathrm{Av}_{\{\alpha_k\}}$ indicates a thermal average over initial vibrational states. The normalized line-shape function $G(\Omega)$ is precisely the same as that for a one-photon transition with 2ω replaced by ω.

The effective electronic operator $(\hat{\boldsymbol{\eta}} \cdot \boldsymbol{R})^2$ in equation (7) may be expressed as a sum of symmetry-adapted operators that transform as bases for irreducible representations of crystallographic point group O_h,

$$\begin{aligned}(\hat{\boldsymbol{\eta}} \cdot \boldsymbol{R})^2 = {} & \tfrac{1}{3}(\eta_x^2 + \eta_y^2 + \eta_z^2)(X^2 + Y^2 + Z^2)\}\mathrm{A}_{1g} \\ & \left.\begin{aligned} +\tfrac{1}{6}(2\eta_z^2 - \eta_x^2 - \eta_y^2)(2Z^2 - X^2 - Y^2) \\ +\tfrac{1}{2}(\eta_x^2 - \eta_y^2)(X^2 - Y^2) \end{aligned}\right\}\mathrm{E}_g \\ & +2\eta_x\eta_y XY + 2\eta_y\eta_z YZ + 2\eta_z\eta_x ZX\}\mathrm{T}_{2g}. \end{aligned} \qquad (9)$$

Equation (9) implies that the ${}^4A_{2g} \rightarrow {}^4T_{2g}$ TPA transition is forbidden, since it could only be mediated by an operator of symmetry T_{1g}. Furthermore, the allowed ${}^4A_{2g} \rightarrow {}^4T_{1g}$ TPA transition, which is mediated by the T_{2g}-symmetry operator in equation (9), must have polarization anisotropy $(2\eta_x\eta_y)^2 = \sin^2(2\phi)$ for light propagating parallel to the z-axis. These conclusions are consistent with the predictions of Bader and Gold [6].

In their investigation of selection rules and polarization anisotropy, Bader and Gold [6] employed an interaction Hamiltonian of the form $\boldsymbol{A} \cdot \boldsymbol{P}$ rather than $\boldsymbol{E} \cdot \boldsymbol{R}$ as employed in the present derivation. Since these two interaction Hamiltonians have the same symmetry properties, predicted selection rules and polarization anisotropy are the same for both. Furthermore, they are related by a gauge transformation, and it can be shown that predicted electric-dipole-transition probabilities in one- and two-photon resonant processes are precisely identical [10]. However, proof of the latter depends on a complete set of intermediate states, including continuum states, on exact eigenfunctions and on the correct expression for the energy denominator. The contributions of individual intermediate states are very different in the two gauges; higher-energy states make a disproportionately greater contribution with $\boldsymbol{A} \cdot \boldsymbol{P}$ (velocity gauge) and lower-energy states with $\boldsymbol{E} \cdot \boldsymbol{R}$ (length gauge). Consequently, approximations such as closure or the assumption of a finite set of intermediate states have different effects in the two gauges. For example, in the approximation of a single intermediate state the ratio of transition probabilities calculated in the velocity and length gauges is $[\omega_{ca}(2\omega - \omega_{ca})/\omega^2]^2$, where $\hbar\omega_{ca}$ is the energy difference between intermediate state c and ground state a. Since the length gauge has been shown to give superior results in approximate two-photon calculations [11], it has been adopted in the present work.

It is evident from the preceding discussion that none of the anomalous features of the TPE spectra reported in I are explained at the level of approximation represented by equations (7)–(9). In order to explain these features, some of the restrictive assumptions adopted above are selectively and independently abandoned in subsequent sections. In particular, we consider the Jahn–Teller effect and departures from the crude adiabatic and closure approximations. The effect of the low-temperature phase transition on the polarization anisotropy is also explored. Finally, hypothetical line-shape simulations are presented to estimate the strengths of coupling to various modes.

2. Jahn–Teller effect

The Born–Oppenheimer approximation is no longer appropriate when the electronic Hamiltonian $H_e(\boldsymbol{Q})$ for fixed nuclear coordinates has degenerate eigenvalues in a symmetrical configuration, which may be adopted as the origin of nuclear coordinates, $\boldsymbol{Q} = \boldsymbol{0}$. This origin is also assumed to be the equilibrium configuration for purely symmetrical displacements.

Symmetry-induced degeneracy is assumed,

$$H_e(\mathbf{0})\phi_n^{(\Gamma)}(\boldsymbol{r},\mathbf{0}) = U^{(\Gamma)}(\mathbf{0})\phi_n^{(\Gamma)}(\boldsymbol{r},\mathbf{0}) \tag{10}$$

where n labels the rows of irreducible representation Γ of the group of the Hamiltonian $H_e(\mathbf{0})$. Changes in the potential $V(\boldsymbol{r},\boldsymbol{Q})$ for small displacements from the symmetrical configuration are treated by degenerate first-order perturbation theory in the harmonic approximation,

$$V(\boldsymbol{r},\boldsymbol{Q}) \cong V(\boldsymbol{r},\mathbf{0}) + \sum_{\Gamma'}\sum_{j}(V_j^{(\Gamma')}Q_j^{(\Gamma')} + \tfrac{1}{2}\omega^{(\Gamma)2}Q_j^{(\Gamma)2}) \tag{11a}$$

$$V_j^{(\Gamma')} \equiv (\partial V/\partial Q_j^{(\Gamma')})_{\boldsymbol{Q}=\mathbf{0}} \tag{11b}$$

where $Q_j^{(\Gamma')}$ the are symmetry-adapted combinations of nuclear displacements (more than one combination may occur with the same symmetry). Matrix elements $\langle\Gamma m|V_j^{(\Gamma')}|\Gamma n\rangle$ between degenerate unperturbed electronic eigenfunctions survive only if the extended Kronecker product representation $\Gamma^* \times \Gamma' \times \Gamma$ contains the identity representation Γ_1. Jahn and Teller [12] showed that each of the 32 crystallographic point groups contains at least one $\Gamma' \neq \Gamma_1$ for every Γ for which this condition is satisfied, and that the matrix is traceless, thus insuring spontaneous distortion limited by the quadratic terms in equation (11*a*). However, the Jahn–Teller theorem makes no prediction concerning the magnitude of this distortion. For that, one must rely on explicit evaluation of matrix elements, facilitated by the point-group analogue of the Wigner–Eckart theorem,

$$\langle\Gamma m|V_j^{(\Gamma')}|\Gamma n\rangle = d_\Gamma^{-1/2}\sum_{\tau_\Gamma}\langle\Gamma\|V^{(\Gamma')}\|\Gamma\rangle\langle\Gamma'\Gamma jn \mid \Gamma\tau_\Gamma m\rangle^* \tag{12}$$

where the coupling coefficient $\langle\Gamma'\Gamma jn \mid \Gamma\tau_\Gamma m\rangle$ is the point-group analogue of a Clebsch–Gordon coefficient [13], d_Γ is the dimension of representation Γ, τ_Γ is the number of times representation Γ occurs in the reduction of the Kronecker product representation $\Gamma' \times \Gamma$, and the reduced matrix element $\langle\Gamma\|V^{(\Gamma')}\|\Gamma\rangle$ is determined by interatomic forces.

The matrix of the Hamiltonian within the degenerate electronic manifold is

$$\mathbf{H} = \mathbf{H}_e + \mathbf{T}_N \tag{13a}$$

$$\begin{aligned}\mathbf{H}_e = {} & [U^{(\Gamma)}(\mathbf{0}) + \tfrac{1}{2}\sum_{\Gamma'}\omega^{(\Gamma')2}\sum_{j}Q_j^{(\Gamma')2}]\mathbf{I} \\ & + d_\Gamma^{-1/2}\sum_{\Gamma'}\sum_{\tau_\Gamma}\langle\Gamma\tau_\Gamma\|V^{(\Gamma')}\|\Gamma\rangle\sum_{j}Q_j^{(\Gamma')}\mathbf{U}_j(\Gamma',\Gamma,\tau_\Gamma)\end{aligned} \tag{13b}$$

$$\mathbf{T}_N = -\tfrac{1}{2}\hbar^2\sum_{\Gamma'}\sum_{j}\frac{\partial^2}{\partial Q_j^{(\Gamma')2}}\mathbf{I} \tag{13c}$$

where $\mathbf{I}$ is the identity matrix and the elements of the matrices $\mathbf{U}_j$ $(\Gamma',\Gamma,\tau_\Gamma)$, which have been tabulated for a number of cases of interest [14], are the coupling coefficients $\langle\Gamma'\Gamma jn \mid \Gamma\tau_\Gamma m\rangle^*$. Adiabatic potential-energy surfaces as functions of the coordinates $Q_j^{(\Gamma')}$, obtained by diagonalizing the electronic Hamiltonian matrix $\mathbf{H}_e$ of equation (13*b*), have been investigated extensively [15]. Minima of these surfaces correspond to stable distortions (static Jahn–Teller effect) in the strong-coupling limit, with energy $-E_{JT}$ with respect to the symmetrical configuration. The nuclear kinetic energy operator $\mathbf{T}_N$ may be treated as a perturbation in this limit, where it gives rise to vibrations about the minima.

The dynamic Jahn–Teller effect prevails in the weak coupling regime, where $\mathbf{H}_e$ and $\mathbf{T}_N$ are comparable [16–18]. The matrices $\mathbf{U}_j$ $(\Gamma',\Gamma,\tau_\Gamma)$ generally do not commute and cannot be diagonalized simultaneously; consequently, the electronic and vibrational motions are inextricably linked in vibronic wave functions,

$$\psi_{n''v}^{(\Gamma'')}(\boldsymbol{r},\boldsymbol{Q}) = \sum_n \phi_n^{(\Gamma)}(\boldsymbol{r},\boldsymbol{0})\theta_{nn''v}^{(\Gamma,\Gamma'')}(\boldsymbol{Q}) = \sum_n \phi_n^{(\Gamma)}(\boldsymbol{r},\boldsymbol{0})\prod_k \chi_{nn''v_k}^{(\Gamma\Gamma'')}(Q_k) \tag{14}$$

with energy eigenvalues

$$E_v^{(\Gamma'')} = U^{(\Gamma)}(0) + \sum_k \varepsilon_{v_k}^{(\Gamma'')} \tag{15}$$

where k denotes (Γ', j). These vibronic wave functions reflect the symmetry of the symmetrical configuration rather than the reduction in symmetry inherent in the static Jahn–Teller effect, since probability is shared among equivalent stable distortions. The TPA transition probability from a non-degenerate ground state to a set of vibronic states derived from a degenerate manifold of electronic states is then

$$W_{a\to\Gamma} = [F(I_0)/\Delta^2]\mathrm{Av}_{\{\alpha_k\}}\sum_{\Gamma''}\sum_{b''}\sum_{\{\beta_k\}}\left|\sum_b \langle\Gamma\mathrm{b}|(\hat{\boldsymbol{\eta}}\cdot\boldsymbol{R})^2|\mathrm{a}\rangle\prod_k\langle\chi_{bb''\beta_k}^{(\Gamma\Gamma'')} \mid \chi_{a\alpha_k}\rangle\right|^2 \times\delta\left[\sum_k(\hbar^{-1}\varepsilon_{\beta_k}^{(\Gamma'')} - \alpha_k\omega_k) - \Omega\right]. \tag{16}$$

3. Phonon-assisted two-photon absorption

Symmetry-forbidden two-photon absorption can be explained as a phonon-assisted process by relaxing the crude adiabatic approximation [7, 8]. The harmonic and closure approximations are retained in the present section, but the dynamic Jahn–Teller effect is invoked in lieu of the Born–Oppenheimer approximation.

The vibronic wave function of equation (14) is the correct linear combination of unperturbed wave functions appropriate to degenerate first-order perturbation theory. The approximation can be improved by a first-order correction to the wave function itself,

$$\psi_{n''v}^{(\Gamma'')}(\boldsymbol{r},\boldsymbol{Q}) = \sum_n \phi_n^{(\Gamma)}(\boldsymbol{r},\boldsymbol{Q})\prod_k \chi_{nn''v_k}^{(\Gamma\Gamma'')}(Q_k) \tag{17a}$$

$$\phi_n^{(\Gamma)}(\boldsymbol{r},\boldsymbol{Q}) \cong \phi_n^{(\Gamma)}(\boldsymbol{r},\boldsymbol{0}) + \sum_k Q_k \sum_{l\neq\Gamma}\frac{\phi_l(r,0)\langle l|V_k|n\rangle}{\hbar(\omega_l-\omega_n)}. \tag{17b}$$

This correction is important when a TPA transition between electronic states is forbidden in the symmetrical configuration; the transition may be enabled by the reduction in symmetry associated with displacements from equilibrium. The TPA transition probability in that case is

$$W_{a\to\Gamma} = [F(I_0)/\Delta^2]\mathrm{Av}_{\{\alpha_k\}}\sum_{\Gamma''}\sum_{b''}\sum_{\{\beta_k\}}\left|\sum_b\sum_q\left[\sum_{l\neq a}(\hbar\omega_{la})^{-1}\langle\Gamma\mathrm{b}|(\hat{\boldsymbol{\eta}}\cdot\boldsymbol{R})^2|l\rangle\langle l|V_q|\mathrm{a}\rangle + \sum_{l\neq\Gamma}(\hbar\omega_{l\Gamma})^{-1}\langle\mathrm{a}|(\hat{\boldsymbol{\eta}}\cdot\boldsymbol{R})^2|l\rangle\langle l|V_q|\Gamma\mathrm{b}\rangle\right]\langle\chi_{bb''\beta_q}^{(\Gamma\Gamma'')}|Q_q|\chi_{a\alpha_q}\rangle \times\prod_{k\neq q}\langle\chi_{bb''\beta_k}^{(\Gamma\Gamma'')}|\chi_{a\alpha_k}\rangle\right|^2\delta\left[\sum_k(\hbar^{-1}\varepsilon_{\beta_k}^{(\Gamma'')} - \alpha_k\omega_k) - \Omega\right]. \tag{18}$$

The zero-phonon line is still forbidden, however, since the lowest vibronic state has the same symmetry as the lowest electronic state from which it is derived [19].

An embedded-cluster model of Cr^{3+}:K_2NaScF_6 [21] suggests that the Jahn–Teller effect in the $^4T_{2g}$ state arises predominantly from coupling to e_g modes. The T × e Jahn–Teller system is a special case in which the $\mathbf{U}_j$ matrices commute and thus can be diagonalized simultaneously [14],

$$\mathbf{U}_\theta = \begin{pmatrix} \frac{1}{2} & 0 & 0 \\ 0 & \frac{1}{2} & 0 \\ 0 & 0 & -1 \end{pmatrix} \tag{19a}$$

$$\mathbf{U}_\varepsilon = \begin{pmatrix} -\frac{1}{2}\sqrt{3} & 0 & 0 \\ 0 & +\frac{1}{2}\sqrt{3} & 0 \\ 0 & 0 & 0 \end{pmatrix}. \tag{19b}$$

Accordingly, each vibronic function is uniquely associated with one of the degenerate electronic functions,

$$\psi_{nv}^{(\Gamma)}(\boldsymbol{r}, \boldsymbol{Q}) = \phi_n^{(\Gamma)}(\boldsymbol{r}, \boldsymbol{Q}) \prod_k \chi_{nv_k}^{(\Gamma)}(Q_k). \tag{20}$$

With the additional simplifying assumptions of random phases and distinct enabling modes, the TPA transition probability then reduces to

$$\begin{aligned} W_{a\to\Gamma} = [F(I_0)/\Delta^2] \sum_b \sum_q \Bigg| &\sum_{l\neq a} (\hbar\omega_{la})^{-1} \langle \Gamma \mathrm{b} | (\hat{\boldsymbol{\eta}} \cdot \boldsymbol{R})^2 | l \rangle \langle l | V_q | \mathrm{a} \rangle \\ &+ \sum_{l\neq\Gamma} (\hbar\omega_{l\Gamma})^{-1} \langle \mathrm{a} | (\hat{\boldsymbol{\eta}} \cdot \boldsymbol{R})^2 | l \rangle \langle l | V_q | \Gamma \mathrm{b} \rangle \Bigg|^2 \\ &\times \sqrt{\frac{\hbar}{2\omega_q}} [(\bar{\alpha}_q + 1) G(\Omega - \omega_q) + \bar{\alpha}_q G(\Omega + \omega_q)] \end{aligned} \tag{21a}$$

$$\bar{\alpha}_q = [\exp(\hbar\omega_q / k_B T) - 1]^{-1} \tag{21b}$$

where a denotes the ${}^4\mathrm{A}_{2g}$ state and Γ denotes the ${}^4\mathrm{T}_{2g}$ state with its three orbitally degenerate components distinguished by b. The only accessible intermediate states $|l\rangle$ are ${}^4\mathrm{T}_{1g}$ states; these may be admixed with the initial state by t_{2g} modes and with the final state by both e_g and t_{2g} modes. Two-photon transitions are then mediated by the E_g and T_{2g} components of $(\hat{\boldsymbol{\eta}} \cdot \boldsymbol{R})^2$ displayed in equation (9). The low-temperature line shape is determined by the normalized line-shape functions $G(\Omega - \omega_q)$, with false origins displaced to higher energy by $\hbar\omega_q$ with respect to the position of the missing zero-phonon line. Since many enabling modes with a range of frequencies are involved, the false origin of the composite TPE band appears as a broad feature rather than as a single sharp line. The absence of a zero-phonon line is guaranteed by the assumption that the enabling modes are distinct from the accepting modes; the final vibronic state must then contain one vibrational quantum of an enabling mode.

The observed magnitude of the displacement of the false origin (I) suggests that the enabling modes may be predominantly e_g modes and the assumption of distinct enabling modes may not be warranted. As an example of indistinct enabling and accepting modes, consider a phonon-assisted transition mediated by a single mode q in the presence of linear coupling to the same mode, as illustrated by the configuration-coordinate diagram of figure 1. The transition probability at $T = 0$ is then of the form

$$W_{a\to b} \propto \sum_\beta |\langle \chi_{b\beta} | Q | \chi_{a0} \rangle|^2 \delta(\beta\omega_q - \Omega) = \left(\frac{\hbar}{2\omega_q}\right) G'(\Omega) \tag{22a}$$

$$G'(\Omega) = \exp(-S) \sum_\beta (\beta - S)^2 (S^{\beta-1}/\beta!) \delta(\beta\omega_q - \Omega). \tag{22b}$$

Note that the zero-phonon line is finite for $S \neq 0$ in this example, in which degenerate modes are disregarded. Nevertheless, as noted previously, it must actually vanish for a forbidden transition between symmetry-adapted vibronic functions when the dynamic Jahn–Teller effect is considered [19]. The normalized line-shape function $G'(\Omega)$ of equation (22*b*) may be compared with the line-shape function $G(\Omega)$ for an allowed transition, equation (8), evaluated for linear coupling to a single mode of frequency ω_0 at $T = 0$, given by [20],

$$G(\Omega) = \exp(-S)\sum_{\beta}(S^{\beta}/\beta!)\delta(\beta\omega_0 - \Omega). \qquad (23)$$

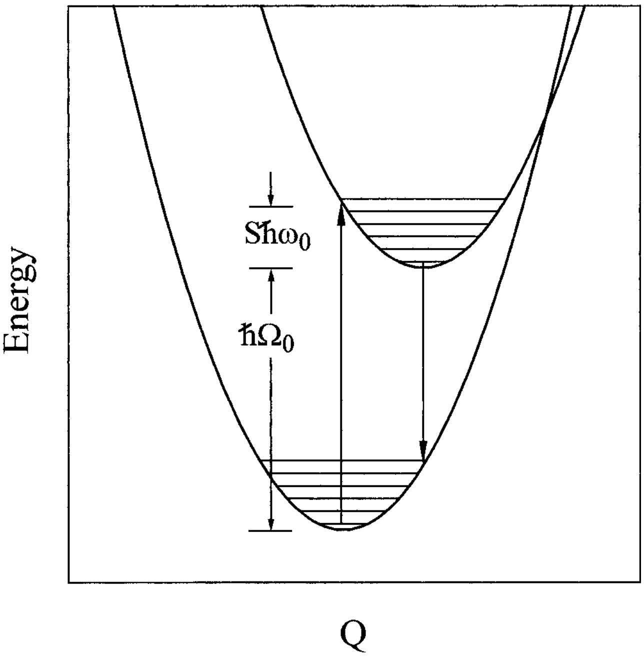

Figure 1. Configuration-coordinate diagram for linear electron–lattice coupling.

4. Anomalously extended progressions

The anomalously extended progressions observed in the ${}^4A_{2g} \rightarrow {}^4T_{1ag}$ TPE spectrum are remarkable both for their resolution and their persistence. Their explanation is to be found by relaxing the closure approximation while retaining the Born–Oppenheimer, harmonic and crude-adiabatic approximations. Since the dynamic Jahn–Teller effect plays no essential role in this explanation, it is ignored in the present section.

We continue to assume a common energy, Δ, for the lowest vibrational state of each intermediate state, but we explicitly include the vibrational energies of intermediate states. (Note that this is precisely opposite to the approximation employed by Honig *et al* [8].) Then the TPA transition probability in this approximation is

$$\begin{aligned} W_{a\rightarrow b} = {} & [F(I_0)/\Delta^2] \times \mathrm{Av}_{\{\alpha_k\}} \sum_{\{\beta_k\}} |\langle \mathrm{b}|(\hat{\boldsymbol{\eta}} \cdot \boldsymbol{R})^2|\mathrm{a}\rangle \prod_k \langle \chi_{b\beta_k} \mid \chi_{a\alpha_k}\rangle \\ & - \sum_c \langle \mathrm{b}|\hat{\boldsymbol{\eta}} \cdot \boldsymbol{R}|\mathrm{c}\rangle\langle \mathrm{c}|\hat{\boldsymbol{\eta}} \cdot \boldsymbol{R}|\mathrm{a}\rangle \sum_{\{\gamma_k\}} \left[\frac{\sum_k \gamma_k\omega_k/\Delta}{1 + \sum_k \gamma_k\omega_k/\Delta}\right] \\ & \times \prod_k \langle \chi_{b\beta_k} \mid \chi_{c\gamma_k}\rangle\langle \chi_{c\gamma_k} \mid \chi_{a\alpha_k}\rangle|^2 \delta\left[\sum_k (\beta_k - \alpha_k)\omega_k - \Omega\right]. \end{aligned} \qquad (24)$$

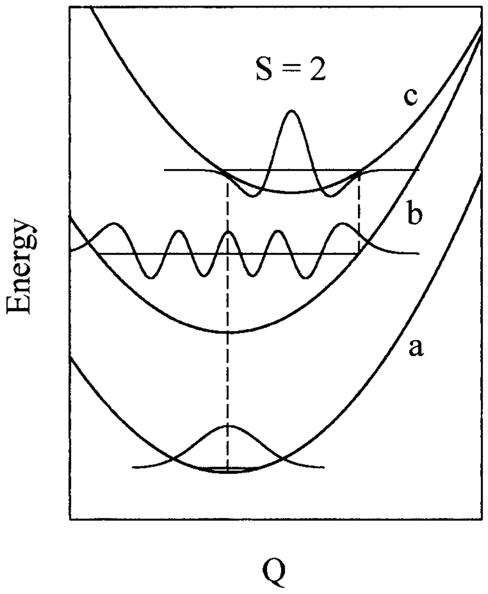

Figure 2. Configuration-coordinate diagram illustrating intermediate-state electron–lattice coupling as a source of extended progressions.

Consider a mode of frequency ω_q, with vibrational quantum numbers α, β and γ, which is linearly coupled to a single diffuse intermediate state $|c\rangle$, but does not directly couple initial and final states. For each value of γ there is a small range of values of β for which $\langle\chi_{b\beta} \mid \chi_{c\gamma}\rangle$ is appreciable, corresponding to coincidence of the classical turning points on the c and b adiabatic potential energy curves, as illustrated in figure 2. Accordingly, we replace the sum over γ and the factor $\langle\chi_{b\beta} \mid \chi_{c\gamma}\rangle$ by the condition

$$\gamma = S + \beta - 2\sqrt{S(\beta + \tfrac{1}{2})} \tag{25a}$$

where S is the Huang–Rhys factor for coupling of states b and c,

$$S = \tfrac{1}{2}\omega^2(Q_0^{(e)} - Q_0^{(b)})^2/\hbar\omega \tag{25b}$$

with $Q_0^{(n)}$ defined by equation (5*b*). Equation (25*a*) is a consequence of the following relations derived from the coincidence of turning points in figure 2:

$$\tfrac{1}{2}\omega^2(Q - Q_0^{(c)})^2 = (\gamma + \tfrac{1}{2})\hbar\omega \tag{25c}$$

$$\tfrac{1}{2}\omega^2(Q - Q_0^{(b)})^2 = (\beta + \tfrac{1}{2})\hbar\omega. \tag{25d}$$

The remaining factor can be evaluated for $\alpha = 0$,

$$\langle\chi_{c\gamma} \mid \chi_{a0}\rangle = (-1)^\gamma \exp(-S/2)\sqrt{S^\gamma/\gamma!}. \tag{26}$$

With the further assumption $\gamma\omega_q/\Delta \ll 1$, coupling to this mode at $T = 0$ introduces an additional progression built on the zero-phonon line,

$$\Delta W_{a\to b} = [F(I_0)/\Delta^2](\omega_q/\Delta)^2|\langle b|\hat{\eta}\cdot\boldsymbol{R}|c\rangle\langle c|\hat{\eta}\cdot\boldsymbol{R}|a\rangle|^2$$
$$\times \prod_{k\neq q} |\langle\chi_{b0_k} \mid \chi_{c0_k}\rangle\langle\chi_{c0_k} \mid \chi_{a0_k}\rangle|^2 \sum_{\beta=0}^{\infty} \exp(-S)(\gamma^2 S^\gamma/\gamma!)\delta(\beta\omega_q - \Omega) \tag{27}$$

where $\gamma(\beta)$ is given by equation (25*a*). The dependence of this expression on β is compared in figure 3 with that of the normalized line-shape function $G(\Omega)$ for linear coupling to a single mode at $T = 0$, equation (23). It is evident that the progression of equation (27) is much more extended than that of equation (23) for a given value of S. Furthermore, the predicted lacuna in the extended progression near $\beta \cong S$ appears to be replicated in the recorded TPE spectrum.

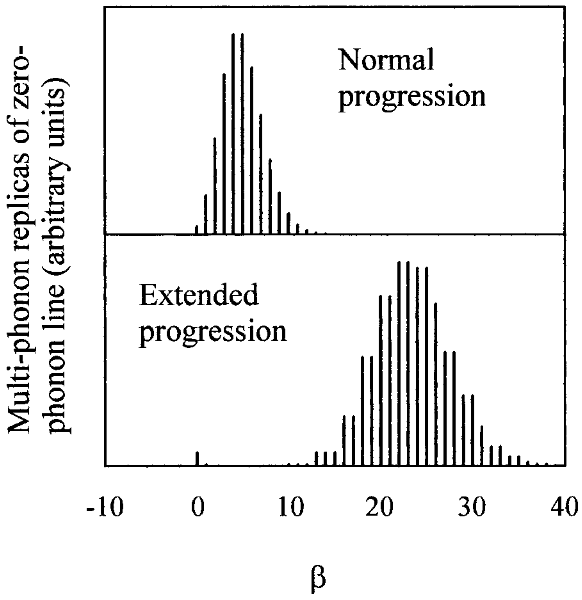

Figure 3. Comparison of a normal progression, equation (23), and an extended progression, equations (25*a*) and (27), for $S = 5$.

Equation (27) implies that the intermediate state must have $^4T_{2u}$ symmetry for a $^4A_{2g} \rightarrow {}^4T_{1ag}$ two-photon transition. Such a state can be constructed as a combination of Slater determinants in which one electron is promoted from a 3d(t_{2g}) orbital (ξ, η or ζ) to a 4p(t_{1u}) orbital (α, β or γ),

$$|^4T_{2u}\xi\tfrac{3}{2}\rangle = \frac{1}{\sqrt{2}}(|\xi_\uparrow\eta_\uparrow\beta_\uparrow| + |\xi_\uparrow\gamma_\uparrow\zeta_\uparrow|) \tag{28a}$$

$$|^4T_{2u}\eta\tfrac{3}{2}\rangle = \frac{1}{\sqrt{2}}(|\xi_\uparrow\eta_\uparrow\alpha_\uparrow| + |\gamma_\uparrow\eta_\uparrow\zeta_\uparrow|) \tag{28b}$$

$$|^4T_{2u}\zeta\tfrac{3}{2}\rangle = \frac{1}{\sqrt{2}}(|\xi_\uparrow\alpha_\uparrow\zeta_\uparrow| + |\beta_\uparrow\eta_\uparrow\zeta_\uparrow|). \tag{28c}$$

The diffuse intermediate state can couple to long-wavelength lattice modes of even parity, including modes of a_{1g}, e_g, t_{1g} and t_{2g} symmetry. The vibration frequencies associated with extended progressions, 106 cm^{-1} and 310 cm^{-1}, must be identified with low-dispersion, zone-centre optical modes in order to explain their persistent resolution. Lattice-mode frequencies measured by Raman scattering [22] and calculated from a lattice-dynamics model [23] are presented in table 1. Local- or resonance-mode frequencies derived from emission spectra in I, also listed in table 1 for comparison, differ little from those of corresponding lattice modes. The most plausible candidates are t_{2g} modes; presumably, the 106 cm^{-1} and 310 cm^{-1} modes associated with extended progressions correspond, respectively, to single components of the $t_{2g}(1)$ and $t_{2g}(2)$ zone-centre modes at 10 K which are coupled to the relevant intermediate states. In a rotated coordinate system with z' axis parallel to $\langle 111\rangle$, the ζ' component of the intermediate-state wave function is

$$\begin{aligned}|^4\mathrm{T}_{2u}\zeta'\tfrac{3}{2}\rangle &= \frac{1}{\sqrt{3}}(|^4\mathrm{T}_{2u}\xi\tfrac{3}{2}\rangle + |^4\mathrm{T}_{2u}\eta\tfrac{3}{2}\rangle + |^4\mathrm{T}_{2u}\zeta\tfrac{3}{2}\rangle)\\ &= \frac{1}{\sqrt{6}}\{|(\beta+\gamma)_\uparrow\eta_\uparrow\zeta_\uparrow| + |\xi_\uparrow(\gamma+\alpha)_\uparrow\zeta_\uparrow| + |\zeta_\uparrow\eta_\uparrow(\alpha+\beta)_\uparrow|\}. \qquad (28d)\end{aligned}$$

The charge distribution of this intermediate-state wave function is conducive to coupling to t_{2g} modes, as illustrated for one Slater determinant in figure 4, unlike those of the initial- and final-state wave functions. The equilibrium configuration for the wave function of equation (28*d*) is a trigonal distortion. Since it follows that the relevant intermediate state is a T × t Jahn–Teller system, with four equivalent energy minima along $\langle 111\rangle$ directions, the heuristic model developed in the preceding paragraph must be oversimplified; nevertheless, it serves to elucidate the nature of anomalously extended progressions.

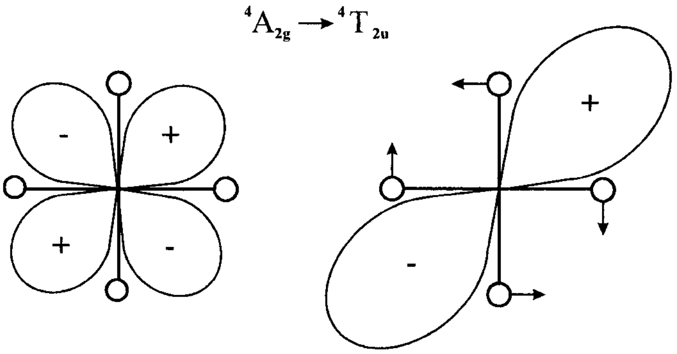

Figure 4. Coupling of a $^4\mathrm{T}_{2u}$ intermediate state to t_{2g} modes. The diagram represents any one of the Slater determinants in equation (28*d*), obtained by 3d → 4p substitution in the initial-state wave function, $|^4\mathrm{A}_{2g}\tfrac{3}{2}\rangle = |\xi_\uparrow\eta_\uparrow\zeta_\uparrow|$. The equilibrium configuration for the $|^4\mathrm{T}_{2u}\zeta'\tfrac{3}{2}\rangle$ intermediate state is a trigonal ($\mathrm{D}_{3\mathrm{d}}$) distortion of the ligand octahedron.

Table 1. Even-parity zone-centre and local-mode frequencies (cm^{-1}) of $\mathrm{K_2NaScF_6}$.

Mode	Raman scattering [22] (^{a}300 K, ^{b}90 K)	Model calculation [23]	Emission spectra (I) (2.1 K)
t_{1g}	inactive^a, 45^b	imaginary	63
$\mathrm{t}_{2g}^{(1)}$	113^a	62.7	121
$\mathrm{t}_{2g}^{(2)}$	250^a	293.6	228
e_g	403^a	453.1	449
a_{1g}	525^a	581.5	542

5. Anomalous polarization anisotropy

The explanation for anomalous polarization anisotropy is to be found in the low-temperature phase transition, ignored in preceding sections, rather than in departures from the simplest approximations. Accordingly, in this section we return to the closure, Born–Oppenheimer, harmonic and crude-adiabatic approximations of equations (7)–(9).

The t_{1g} mode is not Raman active in the high-temperature phase [22]. It softens at low temperature, precipitating a phase transition that presumably stabilizes its frequency and may enable it to become Raman active. The room-temperature Raman line corresponding to the low-frequency t_{2g} mode at 113 cm^{-1} splits into several components in the low-temperature (90 K) Raman spectrum [22], with frequencies ranging from 93 cm^{-1} to 135 cm^{-1}, while a new line appears at 45 cm^{-1}. The low-temperature emission spectrum (2.1 K) (I) reveals a prominent line at 63 cm^{-1} with a shoulder at 121 cm^{-1} that cannot be resolved further. Apart from the temperature difference, the Raman spectrum reflects zone-centre lattice modes while the emission spectrum reflects local and resonance modes associated with the impurity. A plausible interpretation is to attribute the 45 cm^{-1} low-temperature Raman line to the lattice t_{1g} mode stabilized by the phase transition, since its frequency appears to increase with diminishing temperature, and to assign the 63 cm^{-1} emission line to a local or resonance t_{1g} mode associated with the embedded CrF_6^{3-} complex. The shoulder in the emission spectrum at 121 cm^{-1} is then assigned to the low-frequency t_{2g} mode; its poor resolution would obscure finer structure such as the components observed in the low-temperature Raman spectrum. These tentative assignments are incorporated in table 1, where designations are those appropriate to the high-temperature phase.

The phase transition in K_2NaScF_6 revealed by low-temperature Raman scattering [22] is also manifest as a split zero-phonon line and split phonon replicas in low-temperature, high-pressure photoluminescence spectra [24]. Splitting is unresolved in low-temperature emission spectra (I) because the higher-energy component of the split excited state is not thermally populated at 2.1 K, but it is clearly evident in the zero-phonon line of the ${}^4A_{2g} \rightarrow {}^4T_{1ag}$ TPE spectrum. A lattice-dynamics model predicts a librational instability involving co-planar counter-rotating displacements of adjoining octahedra, as shown in figure 5, and a lattice-statics model predicts an equilibrium rotation angle of $\phi_0 = 19.8^\circ$ [23]. This type of instability is peculiar to the perovskite structure, in which the anions have only twofold coordination. The restoring forces are positive in the low-temperature phase, but the librational (t_{1g}) mode is expected to be very soft by virtue of the diminished steric constraints. (For clarity, we will continue to identify modes by their designations in the high-temperature phase.) The energy levels of the CrF_6^{3-} complex are insensitive to a rigid rotation of the complex, but displaced ions beyond the immediate ligands produce a crystal field of symmetry C_{4h} that removes the orbital degeneracy of the ${}^4T_{1ag}$ state. Although point group C_{4h} is Abelian, time-reversal invariance imposes residual degeneracy, leaving a non-degenerate state and a doubly degenerate state, thus splitting the zero-phonon line into two components of unequal intensity.

After averaging over domain orientations, the predicted polarization anisotropy for exciting light propagating along $\langle 100 \rangle$ is given by

$$I(\phi)/I_0^2 \propto 4\sin^2(2\phi) + \sin^2[2(\phi - \phi_0)] + \sin^2[2(\phi + \phi_0)] \tag{29a}$$

with intensity ratio

$$R(\phi_0) \equiv I_{max}/I_{min} = \frac{2 + \cos^2(2\phi_0)}{\sin^2(2\phi_0)}. \tag{29b}$$

The value of this ratio for the predicted rotation is $R(19.8^\circ) = 6.38$, in satisfactory agreement with the value of the ratio observed for the broad side band of the ${}^4A_{2g} \rightarrow {}^4T_{1ag}$ TPE spectrum (I), $R(\phi_0) = 9.0$, corresponding to $\phi_0 = 16.6^\circ$. However, the ratio observed for the zero-phonon line is substantially less, $R(\phi_0') = 2.35$, corresponding to an increased rotation angle of $\phi_0' = 35.6^\circ$.

The increased rotation angle for the zero-phonon transition can be understood as coupling to a soft t_{1g} mode. As noted above, the energy levels of the CrF_6^{3-} complex are insensitive to a rigid rotation of the complex, but coupling can arise as an indirect effect of the excitation.

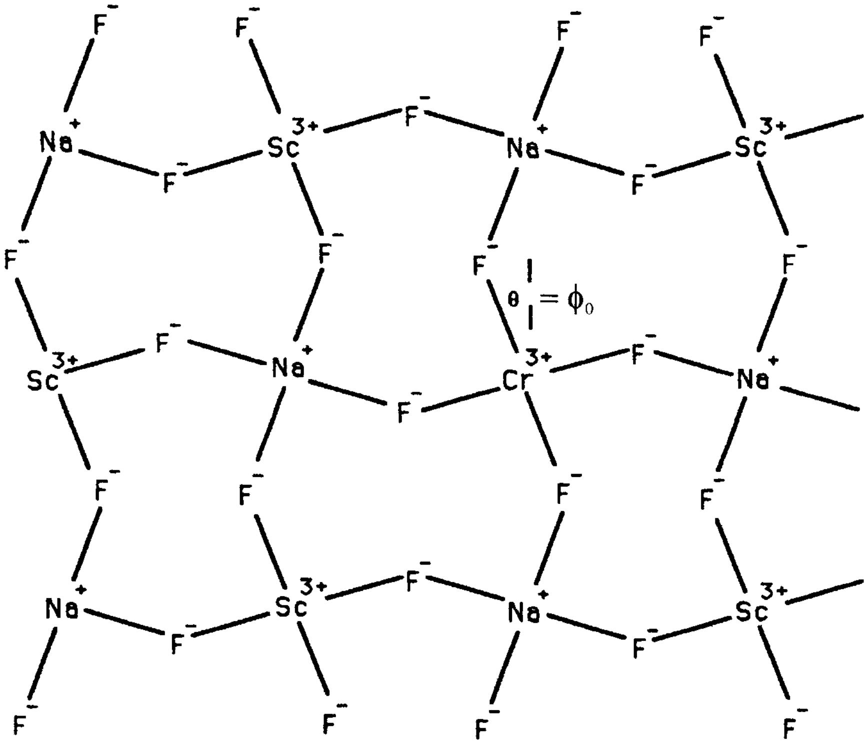

Figure 5. Low-temperature phase transition of Cr^{3+}:K_2NaScF_6 induced by librational instability.

From the viewpoint of ligand-field theory, one electron is promoted from a non-bonding orbital to an anti-bonding orbital in a $^4A_{2g} \to {}^4T_{1ag}$ transition; consequently, metal–ligand bonds are stretched and the rotation angle is increased to accommodate them. Since the $^4A_{2g}$ ground state is transformed to a linear combination of $^4A_{2g}$ and ^4E_g states in a rotated coordinate system appropriate to the $^4T_{1ag}$ excited state, and a TPA transition from each of these states is mediated only by the T_{2g} operator of equation (9), it follows that the polarization anisotropy of the zero-phonon line is governed by the final-state configuration characterized by the angle $\phi_0' = 35.6°$. This configuration governs the polarization anisotropy for transitions to all $^4T_{1ag}$ vibronic states associated with the lowest a_{1g} and e_g vibrational states, as well, since the stretching of metal–ligand bonds is manifest as a combination of a_{1g} and e_g distortions of the CrF_6^{3-} complex. On the other hand, the peak of the broad side band corresponds to a vertical transition on a configuration-coordinate diagram, and thus it reflects only the initial-state configuration with $\phi_0 = 16.6°$. Note that bond stretching alone, which reduces the symmetry of the complex from O_h to D_{4h}, does not affect the polarization anisotropy of the transition in question [6].

6. Line-shape simulations

Hypothetical line-shape functions are developed in the present section, informed where possible by conclusions of preceding sections, to estimate the strength of coupling to various modes in each excited state. The closure, Born–Oppenheimer and harmonic approximations are retained but departure from the crude-adiabatic approximation is invoked for phonon-assisted transitions.

The normalized line-shape function $G(\Omega)$ for linear coupling to a single mode, equation (23), has the property that the area under the zero-phonon line is $\exp(-S)$, where S is the Huang–Rhys factor at $T = 0$. In addition, the first and second moments of $G(\Omega)$ are given by [25]

$$\langle\Omega\rangle = S\omega_0 \tag{30a}$$

$$\langle(\Omega - \langle\Omega\rangle)^2\rangle = S\omega_0^2 \tag{30b}$$

where ω_0 is the angular frequency of vibration. Taken together, these properties provide three relations connecting the two parameters S and ω_0, which are thus over-determined.

Approximate areas and moments derived from the ${}^4A_{2g} \rightarrow {}^4T_{1ag}$ TPE spectrum, averaged over polarizations, yield grossly inconsistent parameter values when analysed according to these relations. The total area of the split zero-phonon line relative to that of the broad band is very small, corresponding to a Huang–Rhys factor $S = 8.9$ (I) and, in combination with the first moment, a phonon frequency $\omega_0 = 324$ cm^{-1}. These values suggest strong coupling to the higher-frequency t_{2g} mode, which could also account for some peculiar line-shape features [26, 27]. We have already invoked strong t_{2g}-mode coupling in intermediate states to explain anomalously extended progressions; however, strong Jahn–Teller coupling to t_{2g} modes in the ${}^4T_{1ag}$ state is considered unlikely [28]. Non-rigid rotation of the chromium hexafluoride complex induced by bond stretching may mediate coupling to t_{2g} bending modes in the final state but it is not expected to make a dominant contribution. On the other hand, the parameter values derived from the combined first and second moments, $S = 6.3$ and $\omega_0 = 459$ cm^{-1}, are more in accordance with expectations for coupling to e_g and a_{1g} modes. The apparent inconsistency is resolved by a model which incorporates simultaneous coupling to several modes. Coupling to a soft t_{1g} mode, evidenced by anomalous polarization anisotropy, generates a relatively narrow line-shape function that serves as a pseudo-zero-phonon line for coupling to e_g and a_{1g} modes. This t_{1g}-mode coupling substantially diminishes the true zero-phonon line while contributing little to the moments of the entire spectrum.

Raman-active, zone-centre modes appear as discrete lines in the Raman spectrum, with apparent line widths limited by instrumental resolution. However, the localized electronic states of the transition-metal impurity are coupled to many modes, with a range of frequencies and wavelengths, corresponding to each of the Raman lines. Thus the widths of the lines in emission and excitation spectra are determined primarily by the projection of the phonon density of states on symmetry-adapted ligand displacements. A model based on the theory of Pryce [29] for linear coupling to many modes can be implemented in the low-temperature limit by adopting an approximate Gaussian single-phonon side band,

$$A(\omega) = -\frac{S}{\sigma\sqrt{2\pi}} \exp[-(\omega - \omega_0)^2/2\sigma^2]. \tag{31a}$$

The normalized line-shape function, resulting from successive convolutions of this single-phonon side band, is given by

$$G(\Omega) = \exp(-S)\left\{\delta(\Omega) + \sum_{\beta=1}^{\infty}\left(\frac{S^\beta}{\beta!}\right)\frac{\exp[-(\Omega - \beta\omega_0)^2/2\beta\sigma^2]}{\sigma\sqrt{2\beta\pi}}\right\} \tag{31b}$$

with each δ-function of equation (23) replaced by a normalized gaussian function of appropriate width. The model can be extended to accommodate coupling to several distinct sets of modes, each with its own single-phonon side band; the composite line-shape function is then simply the convolution of the component line-shape functions.

The simulated line-shape function for the ${}^4A_{2g} \rightarrow {}^4T_{1ag}$ transition shown in figure 6 was constructed as a three-mode convolution by application of this model with the parameter values

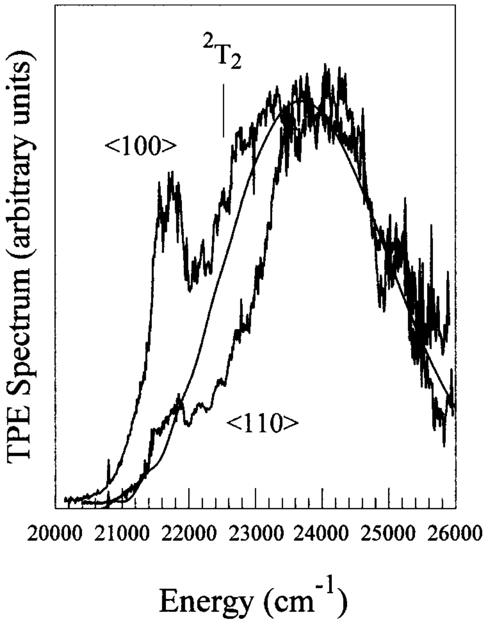

Figure 6. The $^4A_{2g} \to {}^4T_{1ag}$ TPE spectra for $\langle 100\rangle$ and $\langle 110\rangle$ polarization compared with a three-mode line-shape simulation based on the parameters of table 2. The position of $^2T_{2g}$ antiresonance is also indicated.

listed in table 2. It is compared in this figure with the recorded $^4A_{2g} \to {}^4T_{1ag}$ TPE spectra. The parameters were adjusted for a compromise fit between the two polarizations, since the simulation takes no account of wavelength-dependent anomalous polarization anisotropy. Although agreement is generally satisfactory, residual discrepancies may be attributable in part to a Fano antiresonance [30] associated with the multiplicity- and symmetry-forbidden $^4A_{2g} \to {}^4T_{2g}$ transition at 22 500 cm^{-1} [31]. This transition is enabled by spin–orbit interaction, since selection rules for double-group representations allow transitions between the resulting fine-structure states mediated by the operators of equation (9). It should be noted that doublet-state energies are determined only approximately from Fano antiresonances in one-photon spectra.

Table 2. Optimized parameters for the $^4A_{2g} \to {}^4T_{1ag}$ three-mode line-shape simulation.

Mode	ω_0 (cm^{-1})	S	σ (cm^{-1})
t_{1g}	63	2.6	60
e_g	449	4.5	120
a_{1g}	542	1.8 (1.76[a])	120

[a] From equations (33) and (34*b*).

The simulated line-shape function for the $^4A_{2g} \to {}^4T_{2g}$ transition shown in figure 7 was constructed as a convolution of an a_{1g} line-shape function of the form of equation (31*b*) with an e_g phonon-assisted line-shape function of the form

$$G'(\Omega) = \exp(-S)\sum_{\beta=1}^{\infty}(\beta - S)^2\left(\frac{S^{\beta-1}}{\beta!}\right)\frac{\exp\lfloor-(\Omega-\beta\omega_0)^2/2\beta\sigma^2\rfloor}{\sigma\sqrt{2\beta\pi}} \tag{32}$$

adapted from equation (22*b*). The zero-phonon line is omitted in equation (32) for consistency with the forbidden transition in the symmetrical configuration (a concession to the dynamical Jahn–Teller effect), and consequently this function is no longer quite normalized. The optimized parameter values are listed in table 3. The simulated line shape is compared in figure 7 with the recorded $^4A_{2g} \rightarrow {}^4T_{2g}$ TPE spectrum. Residual discrepancies may be attributable in part to Fano antiresonances associated with multiplicity-forbidden $^4A_{2g} \rightarrow {}^2F_g$ and $^4A_{2g} \rightarrow {}^2T_{1g}$ transitions at 15 400 cm^{-1} and 16 300 cm^{-1}, respectively [31].

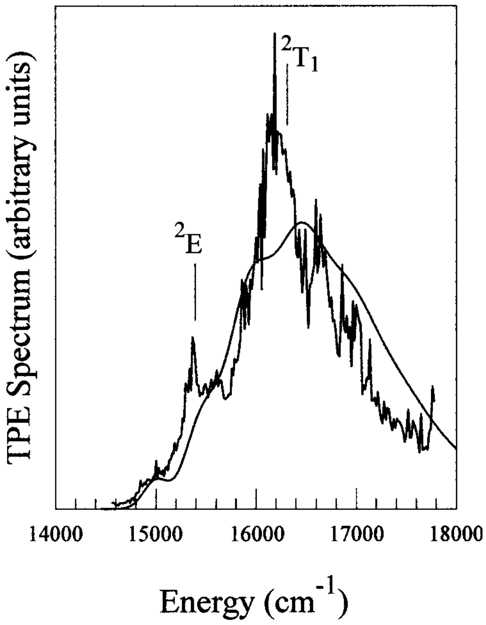

Figure 7. The $^4A_{2g} \rightarrow {}^4T_{2g}$ TPE spectrum for ⟨100⟩ polarization compared with a two-mode phonon-assisted line-shape simulation based on the parameters of table 3. The positions of ^2E_g and $^2T_{1g}$ antiresonances are also indicated.

Table 3. Optimized parameters for the $^4A_{2g} \rightarrow {}^4T_{2g}$ two-mode, phonon-assisted line-shape simulation.

Mode	ω_0 (cm^{-1})	S	σ (cm^{-1})
e_g	449	1.3 (0.95[a])	120
a_{1g}	542	0.9 (0.76[a], 1.26[b])	120

[a] [21].
[b] from equation (33) and (34*a*).

The optimized parameter values listed in tables 2 and 3 can be related to the Tanabe–Sugano energy-level diagram for this system, shown in figure 1 of (I). A configuration-coordinate diagram for coupling to an a_{1g} mode can be constructed from the Tanabe–Sugano diagram by re-plotting the energy levels as functions of the configuration coordinate Q for symmetrical displacements of the octahedron, provided the dependence of Dq on Q is known [31]. With the assumption of a point-charge model for the crystal field, the required dependence is $Dq \propto Q^{-5}$. The elastic energy associated with displacements from the ground-state equilibrium configuration Q_0 must be added in order to obtain the adiabatic-potential-energy curves. If one assumes that this additional elastic energy is the same for all states and depends quadratically on $Q - Q_0$, and if one further neglects that part of the curvature of each excited-state adiabatic-potential-energy curve derived from the Tanabe–Sugano diagram, which is indeed negligible in comparison with the curvature of the elastic energy, then linear coupling is preserved and only the phonon energy $\hbar\omega_0$ is required in order to complete the configuration-coordinate diagram. The zero-temperature Huang–Rhys factor is then given by

$$S = \left(\frac{25}{12}\right) \frac{(Dq_0)^2}{\hbar\omega_0^3 M r_0^2} \left(\left.\frac{\mathrm{d}E}{\mathrm{d}Dq}\right|_{Q=Q_0} \right)^2 \tag{33}$$

where $r_0 = Q_0/\sqrt{6M}$ is the equilibrium metal–ligand distance and M is the mass of one ligand ion. The energies of the relevant states are given as functions of Dq by [32]

$$E(^4T_2) = 10Dq \tag{34a}$$

$$E(^4T_{1a}) = 15Dq + \tfrac{15}{2}B - \tfrac{1}{2}\sqrt{100(Dq)^2 - 180DqB + 225B^2}. \tag{34b}$$

Values of S for the a_{1g} mode, calculated from equations (33) and (34) with the parameter values of table 4, are listed in tables 2 and 3 for comparison. Values of S inferred from *ab initio* embedded cluster calculations of Stokes shifts and phonon frequencies [21] are also listed in table 3.

Table 4. Parameter values for K_2NaScF_6:Cr^{3+} [31].

Parameter	Value
B	794 cm^{-1}
C/B	4.07
Dq_0	1560 cm^{-1}
$\hbar\omega_0^{a}$	542 cm^{-1}
r_0^{b}	2.12 Å
M	3.154×10^{-26} kg

[a] From I.

[b] One-quarter of the lattice parameter.

It is evident from table 3 that the optimized values of S for the $^4A_{2g} \rightarrow {}^2T_{2g}$ TPE spectrum are consistent with values from equations (33) and (34*a*), derived from the Tanabe–Sugano diagram, figure 1 of I. They are somewhat larger than the predictions of *ab initio* calculations [21], for which the simulated lattice is known to be too rigid. The simulation of the $^4A_{2g} \rightarrow {}^2T_{1ag}$ TPE spectrum by a three-mode convolution involves too many adjustable parameters for a unique fit. Accordingly, the Huang–Rhys factors in table 2 were constrained by equations (33) and (34*b*) and by the requirement, imposed by the relative area of the zero-phonon line, that their sum equal 8.9.

A simple model for t_{1g}-mode linear coupling in the harmonic approximation based on hindered rotation of a rigid CrF_6^{3-} complex predicts the relation

$$\Delta\phi_0 = \sqrt{\hbar S/(2Mr_0^3\omega_0)} \tag{35}$$

where $\Delta\phi_0 = \phi_0' - \phi_0$ is the difference of equilibrium rotation angles between the $^4T_{1ag}$ and $^4A_{2g}$ states. With the parameter values listed in tables 2 and 4, equation (35) yields $\Delta\phi_0 = 5^\circ$ rather than the value of 19° inferred from anomalous polarization anisotropy in section 5. This discrepancy suggests significant non-linear and/or anharmonic coupling.

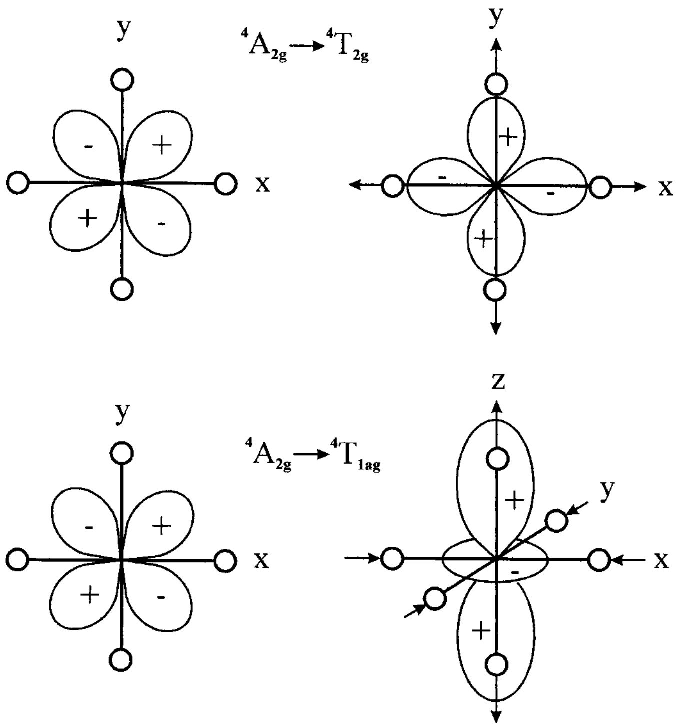

Figure 8. Coupling of ${}^4\mathrm{T}_{2g}$ and ${}^4\mathrm{T}_{1ag}$ final states to e_g modes. The diagrams represent the wave functions of equations (36) as obtained by substitution from the initial-state wave function, $|{}^4\mathrm{A}_{2g}\frac{3}{2}\rangle = |\xi_\uparrow\zeta_\uparrow\zeta_\uparrow|$. It is evident that the e_g displacements are of opposite sign in the two final states.

7. Summary and conclusions

Unexpected features of Cr^{3+}:$\mathrm{K_2NaScF_6}$ TPE spectra, excited by a Raman-shifted, Nd:YAG-pumped tunable dye laser, are explained by theoretical models. To explain these features, some of the restrictive assumptions of the closure, Born–Oppenheimer, harmonic and crude-adiabatic approximations are selectively and independently abandoned. In particular, the Jahn–Teller effect and departures from the crude-adiabatic and closure approximations are invoked, and the effect of the low-temperature phase transition is explored.

A weak TPE spectrum of the symmetry-forbidden ${}^4\mathrm{A}_{2g} \rightarrow {}^2\mathrm{T}_{2g}$ transition, observed without a zero-phonon line, is attributed to phonon assistance. Anomalously extended vibrational progressions in the symmetry-allowed ${}^4\mathrm{A}_{2g} \rightarrow {}^2\mathrm{T}_{1ag}$ TPE spectrum are understood in terms of electron–lattice coupling in intermediate states, obscured in the closure approximation. An anomalously weak, split zero-phonon line of the ${}^4\mathrm{A}_{2g} \rightarrow {}^2\mathrm{T}_{1ag}$ TPE spectrum and anomalous polarization anisotropy are consequences of a low-temperature phase transition. Hypothetical line-shape simulations fitted to observed TPE spectra provide the optimized parameter values listed in tables 2 and 3.

The strength of coupling to the e_g mode is much greater in the ${}^4\mathrm{T}_{1ag}$ state than in the ${}^4\mathrm{T}_{2g}$ state. Furthermore, one can infer from the contrasting charge distributions of their wave functions,

$$|{}^4\mathrm{T}_{2g}\zeta\tfrac{3}{2}\rangle = |\xi_\uparrow\eta_\uparrow\varepsilon_\uparrow| \tag{36a}$$

$$|{}^4\mathrm{T}_{1ag}\gamma\tfrac{3}{2}\rangle = |\xi_\uparrow\eta_\uparrow\theta_\uparrow| \tag{36b}$$

that their equilibrium e_g displacements are in opposite directions, as illustrated in figure 8. The excited-state absorption (ESA) band is broadened as a consequence of these opposing displacements [33–35].

Acknowledgments

This work was supported by the US Army Research Office under contract no DAAL03-89-K-0059. The authors are grateful to Professor Donald McClure for helpful discussions. They also acknowledge a useful suggestion by a referee concerning the optimum choice of gauge.

References

[1] Wein G R, Hamilton D S, Sliwczuk U, Rinzler A G and Bartram R H 2001 *J. Phys.: Condens. Matter* **13** 2363

[2] Göppert-Mayer M 1931 *Ann. Phys.* **9** 273

[3] Kaiser W and Garrett C G B 1961 *Phys. Rev. Lett.* **7** 229

[4] Axe J D Jr 1964 *Phys. Rev.* A **136** 42

[5] Inoue M and Toyozawa Y 1965 *J. Phys. Soc. Japan* **20** 363

[6] Bader T R and Gold A 1968 *Phys. Rev.* **171** 997

[7] Gold A and Hernandez J P 1965 *Phys. Rev.* A **139** 2002

[8] Honig B, Jortner J and Szöke A 1967 *J. Chem. Phys.* **46** 2714

[9] Born M and Oppenheimer J R 1927 *Ann. Phys., Lpz.* **84** 457

[10] Cohen-Tannoudji C, Dupont-Roc J and Grynberg G 1989 *Photons and Atoms* (New York: Wiley–Interscience) pp 316–24

[11] Bassani F, Forney J J and Quattropani A 1977 *Phys. Rev. Lett.* **39** 1070

[12] Jahn H A and Teller E 1937 *Proc. R. Soc.* A **161** 220

[13] Koster G F, Dimmock J O, Wheeler R G and Statz H 1963 *Properties of the Thirty-Two Point Groups* (Cambridge, MA: MIT Press)

[14] Ham F S 1972 Jahn–Teller effects in electron paramagnetic resonance spectra *Electron Paramagnetic Resonance* ed S Geschwind (New York: Plenum) pp 1–119

[15] Liehr A D 1963 *J. Phys. Chem.* **67** 389

[16] Moffitt W and Liehr A D 1957 *Phys. Rev.* **106** 1195

[17] Moffitt W and Thorson W 1957 *Phys. Rev.* **108** 1251

[18] Longuet-Higgins H C, Öpik U, Pryce M H L and Sack R A 1958 *Proc. R. Soc.* A **244** 1

[19] Ham F S 1965 *Phys. Rev.* A **138** 1727

[20] Huang K and Rhys A 1950 *Proc. R. Soc.* A **204** 406

[21] Woods A M, Sinkovits R S, Charpie J C, Huang W L, Bartram R H and Rossi A R 1993 *J. Phys. Chem.* **54** 543

[22] Sliwczuk U, Bartram R H, Gabbe D R and McCollum B C 1991 *J. Phys. Chem.* **52** 357

[23] Sinkovits R S and Bartram R H 1991 *J. Phys. Chem.* **52** 1137

[24] Dolan J F, Rinzler A G, Kappers L A and Bartram R H 1992 *J. Phys. Chem.* **53** 905

[25] Lax M 1952 *J. Chem. Phys.* **20** 1752

[26] Cho K 1968 *J. Phys. Soc. Japan* **25** 1372

[27] Englman R 1972 *The Jahn–Teller Effect in Molecules and Crystals* (London: Wiley–Interscience)

[28] Sturge M D 1967 The Jahn–Teller effect in solids *Solid State Physics* vol 20, ed F Seitz, D Turnbull and H Ehrenreich (New York: Academic) pp 92–211

[29] Pryce M H L 1966 Interactions of lattice vibrations with electrons at point defects *Phonons* ed R W H Stevenson (New York: Plenum) pp 403–48

[30] Sturge M D, Guggenheim H J and Pryce M H L 1970 *Phys. Rev.* B **2** 2459

[31] Andrews L J, Lempicki A, McCollum B C, Giunta C J, Bartram R H and Dolan J F 1986 *Phys. Rev.* B **34** 2735

[32] Sugano S, Tanabe Y and Kamimura H 1970 *Multiplets of Transition-Metal Ions in Crystals* (New York: Academic)

[33] Andrews L J, Hitelman S M, Kokta M and Gabbe D 1986 *J. Chem. Phys.* **84** 5229

[34] Caird J A, Payne S A, Staver P R, Ramponi A J, Chase L L and Krupke W F 1988 *IEEE J. Quantum Electron.* **24** 1077

[35] Lee H W H, Payne S A and Chase L L 1989 *Phys. Rev.* B **39** 8907